machines

MDPI

Article

Mechanism Design of a Novel Device to Facilitate Mobility, Sit-to-Stand Transfer Movement, and Walking Assistance

Bo Li, Xinzhili Chen *, Hailiang Liu, Dong Yuan, Jiafeng Zhang and Shiqing Lu

College of Mechanical Engineering, Chongqing University of Technology, Chongqing 400054, China; libo2018@cqut.edu.cn (B.L.); liuhailiang@stu.cqut.edu.cn (H.L.); xiaoyuan@stu.cqut.edu.cn (D.Y.); 52231206138@stu.cqut.edu.cn (J.Z.); shiqing.lu@cqut.edu.cn (S.L.)

* Correspondence: 51221201129@stu.cqut.edu.cn

Abstract: To assist patients with lower limb dysfunction in mobility, standing, and walking, this paper proposes a novel device that integrates the functions of lower limb exoskeleton, wheelchair, and sit-to-stand (STS) transfer assistance. We designed a 10-degree-of-freedom lower limb exoskeleton based on gait analysis. To satisfy human–machine compatibility, the hip joint was conceptualized as a remote center-of-motion (RCM) mechanism, the knee joint was developed as a cam mechanism, and the ankle joint was designed as a revolute pair. We constructed a kinematic model of the exoskeleton by adopting the product-of-exponential (POE) formula. The STS transfer assistance mechanism was designed based on Stephenson III six-bar linkage through path synthesis methods. The length of this six-bar mechanism was determined based on using Newton–Jacobi iterative techniques. We connected the STS assistive mechanism to the wheelchair frame, and then, we connected the exoskeleton to the STS transfer assistive mechanism. The experimental results demonstrated that the STS assistance path aligned closely with human buttock trajectories, and the walking assistance paths corresponded with natural human gaits. This device produces a new choice for patients with lower limb dysfunction.

Keywords: lower limb exoskeleton; sit-to-stand assistive mechanism; compatibility design; path synthesis; Stephenson III six-bar linkage; product-of-exponential formula

check for updates

Academic Editor: Zhuming Bi

Received: 26 December 2024
Revised: 21 January 2025
Accepted: 27 January 2025
Published: 10 February 2025
Corrected: 11 September 2025

Citation: Li, B.; Chen, X.; Liu, H.; Yuan, D.; Zhang, J.; Lu, S. Mechanism Design of a Novel Device to Facilitate Mobility, Sit-to-Stand Transfer Movement, and Walking Assistance. *Machines* **2025**, *13*, 134. https://doi.org/10.3390/machines13020134

Copyright: © 2025 by the authors. Licensee MDPI, Basel, Switzerland. This article is an open access article distributed under the terms and conditions of the Creative Commons Attribution (CC BY) license (https://creativecommons.org/licenses/by/4.0/).

1. Introduction

Lower limb dysfunction is a type of physical disability that arises from unhealthy lifestyle choices or medical conditions such as stroke and spinal cord injury. Patients experiencing lower limb dysfunction often encounter challenges in performing daily activities, including moving, standing, and walking [1]. To assist patients in completing these activities and to enhance their life quality, it is essential to provide appropriate assistive devices for them.

Wheelchairs are served as the primary equipment utilized to aid patients with lower limb dysfunction. While wheelchairs significantly improve patient's mobility, they restrict patients to a seated position. Patients who maintain a seated position for a long time are at increased risk of developing various complications, including pressure ulcers and urolithiasis [2,3]. Motion training such as standing or walking facilitates improvements or the restoration of lower limb function [4,5]. Although there has been research on wheelchairs to assist patients in standing, studies on wheelchairs intended to aid patients in walking remain scarce [6–8].

Lower limb exoskeletons have been used to assist individuals with lower limb dysfunction in walking. The structural design of these exoskeletons should be compatible with

patients to facilitate flexible and comfortable movement. Exoskeletons such as ReWalk [9], Ekso [10], and Indego [11] maintain the sagittal plane's rotational degrees of freedom (DOFs) for the hip, knee, and ankle joints. These devices enable patients to move along the sagittal plane by facilitating the rotation of the hip and knee joints. However, the simplification of hip and ankle joint structures in these exoskeletons often results in inadequate balance support and an unnatural gait [12]. In contrast, other exoskeletons like REX [13], ATANLANTE [14], and AutoLEE-II [15] offer users more natural gait patterns along with self-balancing capabilities. However, the complex structure of these exoskeletons rendered them excessively heavy, resulting in a slower walking pace.

The integration of exoskeletons and wheelchairs enhances the stability of walking assistance and simplifies the structure of walking and moving devices. However, these devices frequently overlook the habitual movements associated with sit-to-stand (STS) movement. Song et al. [16] developed a robot that combined a wheelchair and an exoskeleton based on a reconfigurable mechanism to assist patients in STS transfers and walking activities. It exhibited instability due to its failure to account for the change in the user's center of gravity during STS transfer movement. Chaichaowarat et al. [17] integrated wheelchair and exoskeleton functionalities while considering the movement of the human body's center of gravity along the support axis during the STS transfer process. It could maintain balance during these actions. Researchers involved in developing such hybrid robots neglected STS movement trajectories, which led to incorrect postures.

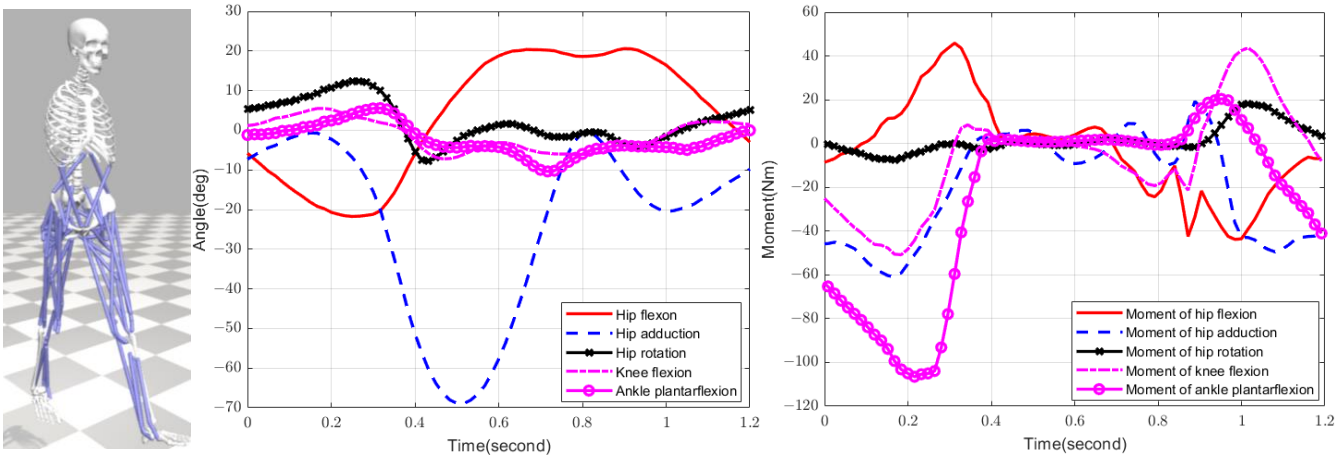
The STS transfer movement is an energy-intensive motion encountered in daily life [18]. Das et al. [19] designed an STS assistive device utilizing a four-bar linkage mechanism with a pushing arm. Zhou et al. [20] developed a 3-DOF-series STS assistive device by elevating the patient's upper limbs. These STS assistive devices imposed high demands on upper limb strength. Users whose upper limb strength was insufficient to support their own body were unable to utilize these devices. Rea et al. [21] developed a device that assists patients by applying force to their buttocks during STS transfers. This design demanded minimal strength on the upper limbs. However, it occupied more space due to its complex structure, and it could interfere with the movement of the lower limbs during walking.

Our research proposed a novel device to assist patients by integrating mobility functions with STS transfer capabilities and walking functionalities. Firstly, we designed a lower limb exoskeleton, and we simulated it to verify its human–machine compatible. Secondly, we designed an STS assistive mechanism based on an analysis of the STS movement process of healthy humans. Then, we integrated the STS assistive mechanism, exoskeleton, and wheelchair. Finally, we conduct three-dimensional (3D) motion capture experiments to validate the assistive effect of the device.

2. Design and Analysis of Lower Limb Exoskeleton

2.1. Analysis of Walking Locomotion

The exoskeleton mechanism is determined by human anatomy and the kinematics of walking. The kinematic and dynamic simulations of walking were conducted by OpenSim 4.3 to illustrate the rotation angles and torques of each joint during walking, as shown in Figure 1 [22]. We adopt five degrees of freedom (DOFs) in level walking locomotion for each lower limb, including flexion/extension at the knee joint; dorsiflexion/plantarflexion at the ankle joint; and flexion/extension, adduction/abduction, and internal/external rotation at the hip joint.



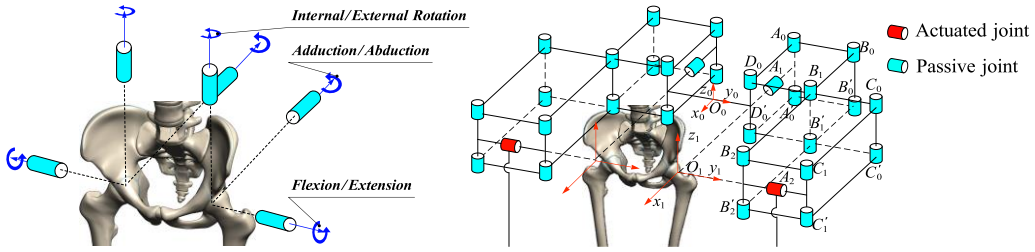
(**a**) (**b**) (**c**)

Figure 1. Gait analysis: (**a**) walking simulation in OpenSim; (**b**) rotation angle of hip, knee, and ankle joints. (**c**) Torque of hip, knee, and ankle joints.

2.2. Compatibility Design of Exoskeleton

2.2.1. Structural Design of Hip Joint

The human hip joint is classified as a ball-and-socket joint [23]. Based on the analysis from Section 2.1, we served the hip joint as three revolute pairs, as shown in Figure 2a. The three revolute pairs are situated on the sagittal, coronal, and horizontal planes. The axes of the three pairs intersect at a point that coincides with the center of the hip joint. The axes corresponding to internal/external rotation DOFs for the exoskeleton hip joint do not align directly with those of the human hip joint. We designed the hip joint based on a remote center-of-motion (RCM) configuration, as shown in Figure 2b. This design ensures motion compatibility between the exoskeleton and human hip joints [24].



(**a**) (**b**)

Figure 2. Configuration synthesis of hip joints: (**a**) three revolute pairs served as hip joints; (**b**) configuration of hip joints.

We designed limit mechanisms based on right-angle torsion springs (wire diameter: 2.5; outer diameter: 18; number of turns: 3; materials: SWRH72A) at points A_0, A_1, and D_0 in order to prevent injuries to the wearer due to excessive movement. We served the DOFs related to flexion/extension as driving degrees of freedom due to their crucial roles in facilitating walking movements. We selected the servo motor MG8016E-i24B (diameter and thickness of $\Phi 80 \times 53.5$, maximum torque of 45 Nm, weight of 1.1 kg, and max speed of 160 rpm) produced in China as the motor of hip flexion/extension required by the moment of hip flexion from Figure 1c. The structure of the hip joint is shown in Figure 3.

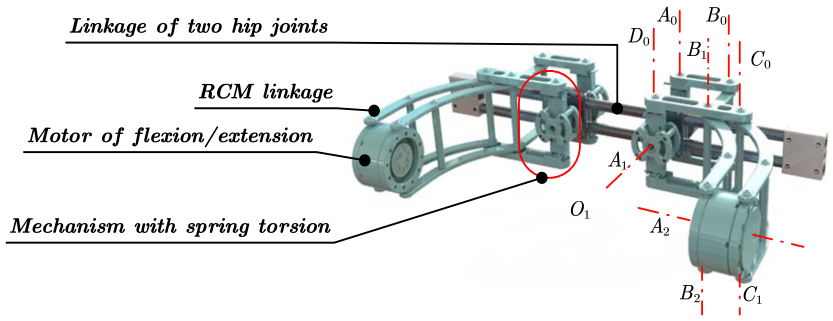


Figure 3. Structure of hip joint.

2.2.2. Structural Design of Knee Joint

The knee joint is the most complex hinge joint in the lower limb [25]. During the motion of the knee joint, the position of the instantaneous center of rotation exhibits a variation that closely resembles a J-curve [26]. To accommodate this curve, we designed a cam mechanism based on paper [27]. The polar coordinate equation of an ellipse to represent the cam groove is presented in Formula (1):

$$r(\theta) = \frac{ab}{\sqrt{(b\cos(\theta))^2 + (a\sin(\theta))^2}}, \quad (1)$$

where θ is the rotation angle, a is the length of the major axis, b is the length of the minor axis, and the radius r is a function of the angle θ. This paper sets a = 45 mm and b = 55 mm, providing a linear displacement of 10 mm.

Based on Formula (1), the knee joint was designed, as shown in Figure 4. The shank rotates around the center of rotation on the cam during knee joint movement, while the roller on the shank slides along the cam groove. The shank stretches within the expansion groove.

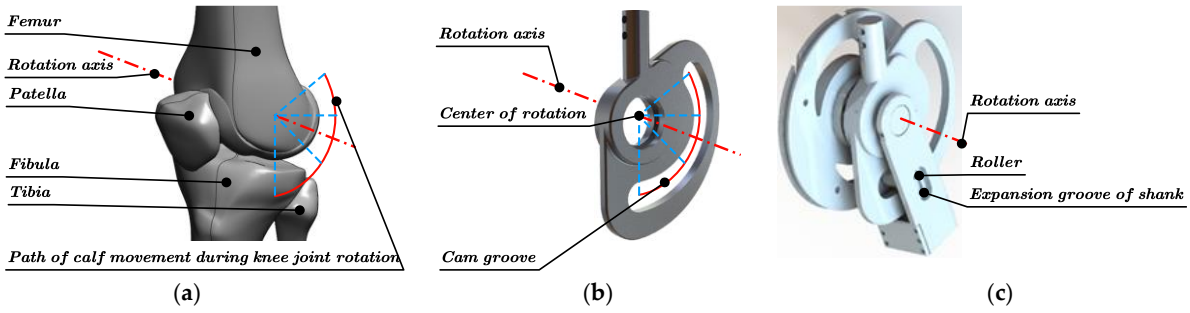


Figure 4. Design of knee joint: (**a**) human knee joint; (**b**) cam mechanism; (**c**) knee joint of exoskeleton.

2.2.3. Structural Design of Ankle Joint

The ankle joint provides plantarflexion/dorsiflexion DOFs in the sagittal plane, as movements occurring in the coronal and horizontal plane have minimal influence on facilitating walking movements [22]. Since the DOFs of foot inversion/eversion are omitted in the exoskeleton design, we designed the foot pad of the exoskeleton with flexible materials (thermoplastic polyurethane, TPU) to enable the human foot to have the DOFs of inversion/eversion. The foot pad is connected to the ankle joint via an adjustable telescopic rod, which accommodates varying ankle heights. The structure of the ankle joint is shown in Figure 5.

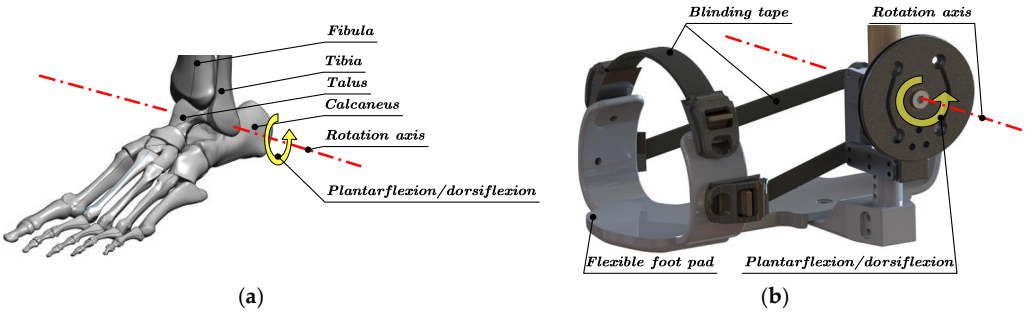


Figure 5. Ankle joint mechanism: (**a**) human ankle; (**b**) ankle joint of exoskeleton.

2.2.4. Structural Design of Exoskeleton Model

The configuration synthesis of the exoskeleton is shown in Figure 6a. Each lower limb of the exoskeleton comprises five DOFs, with three active DOFs designated for driving hip, knee, and ankle joints to realize flexion/extension. Additionally, the internal/external rotations of the hip joint, as well as adduction/abduction at the hip joint, are classified as passive DOFs.

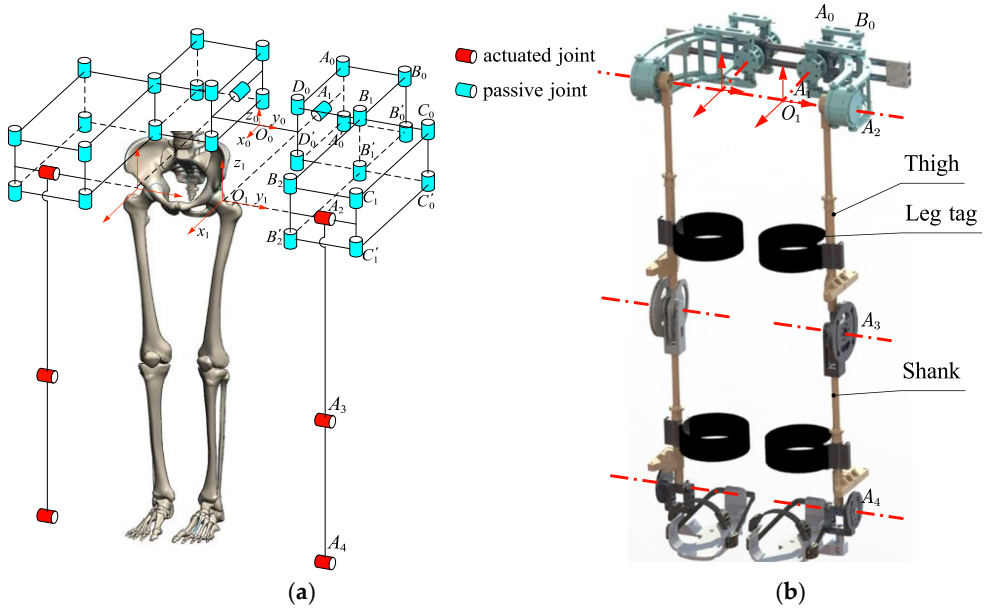


Figure 6. Exoskeleton model: (**a**) configuration of the exoskeleton; (**b**) mechanism design of the exoskeleton.

The model of the mechanical structure is shown in Figure 6b. The exoskeleton does not provide a self-balancing function, which would be provided by the wheelchair, as discussed later. To create a light-weight exoskeleton to reduce the burden of walking assistance, we mainly utilized aluminum alloy 6061 to create the ankle joint mechanism, and we chose the carbon-fiber-reinforced plastics (CFRPs) to create the exoskeleton's thigh and shank. In addition, based on Figure 1c, we chose MG8016E-i24B to drive the knee and ankle joints with a 3:1 drive ratio through a rope drive. Both the thigh and calf are telescopic tubes for which their lengths can be adjusted. Based on the standard titled Human dimensions of Chinese adults, the range of the size of the shank is between 297 mm and 434 mm, and the range of the size of the thigh is between 375 mm and 537 mm, which matches the length of different human lower limbs. The left lower limbs and the right lower limbs are connected by an adjustable connection linkage, which can adjust the exoskeleton's hip width from 281 mm to 382 mm to match different adults. The leg tags, which are designed using nylon, are set on the thighs and shanks for the patient to wear.

2.3. Kinematical Analysis of the Exoskeleton

2.3.1. Forward Kinematics

The configuration of the exoskeleton is simplified to facilitate the development of the kinematics model, as shown in Figure 7. The knee joint is divided into a revolute pair and a prismatic pair. The standing state is considered as the initial state of the exoskeleton for determining its motion space. The base coordinate system $\{S\}$ is defined at the hip joint of the exoskeleton, while the tool coordinate system $\{T\}$ is established at the foot. The kinematics model for each lower limb of the exoskeleton is formulated based on the product of the exponential (POE) formula [28]. l_0 represents the distance from the center of the human hip joint to the thigh of the exoskeleton. l_1 and l_2 represent the length of thigh and shank. l_3 represents the ankle height. θ_i represents the rotation angle of the ith revolute pair, p_1 denotes displacement associated with the prismatic pair, $g_{st}(\mathbf{0})$ represents initial pose of $\{T\}$, i.e., standing position, and $g_{st}(\boldsymbol{\theta})$ signifies pose transformation from $\{T\}$ to $\{S\}$, where $\boldsymbol{\theta} = (\theta_1, \theta_2, \ldots \theta_n)$. Additionally, $\hat{\xi}_i$ denotes the spinor for each revolute pair. Consequently, we express the tool pose through POE formulation; we refer to Formula (2):

$$\begin{cases} g_{st}(\boldsymbol{\theta}) = e^{[\hat{\xi}_1]\theta_1} e^{[\hat{\xi}_2]\theta_2} e^{[\hat{\xi}_3]\theta_3} e^{[\hat{\xi}_4]\theta_4} e^{[\hat{\xi}_5]\theta_5} e^{[\hat{\xi}_6]p_1} g_{st}(\mathbf{0}) \\ \left[\hat{\xi}_i\right] = \begin{pmatrix} \left[\hat{\omega}_i^T\right] & (\boldsymbol{r}_i \times \hat{\omega}_i)^T \\ \mathbf{0} & 0 \end{pmatrix} (i = 1,\ 2,\ 3,\ 4,\ 5) \\ \hat{\xi}_i = \left(\hat{\omega}_i^T,\ (\boldsymbol{r}_i \times \hat{\omega}_i)^T\right)^T (i = 1,\ 2,\ 3,\ 4,\ 5) \\ \left[\hat{\xi}_6\right] = \begin{pmatrix} \mathbf{0} & \hat{v}_1^T \\ \mathbf{0} & 0 \end{pmatrix} \\ \hat{\xi}_6 = \left(\mathbf{0}, \hat{v}_1^T\right)^T \end{cases}, \tag{2}$$

where $\hat{\omega}_i$ is the unit vector in the direction of the rotational angular velocity of the revolute joint. $\hat{v}_1$ is the unit vector in the direction of the translational velocity of the prismatic joint. $\left[\hat{\omega}_i^T\right]$ is the anti-symmetric matrix of $\hat{\omega}_i^T$. $\boldsymbol{r}_i$ is the radius vector of each revolute pair relative to the base coordinate system. The vector expression of $\hat{\omega}_i$ and $\hat{v}_1$ is shown in Formula (3), and the expression of $\boldsymbol{r}_i$ is shown in Formula (4).

$$\begin{cases} \hat{\omega}_3 = \hat{\omega}_4 = \hat{\omega}_5 = (0,\ 1,\ 0)^T \\ \hat{\omega}_1 = (1,\ 0,\ 0)^T \\ \hat{\omega}_2 = \hat{v}_1 = (0,\ 0, -1)^T \end{cases}, \tag{3}$$

$$\begin{cases} \boldsymbol{r}_1 = \boldsymbol{r}_2 = \boldsymbol{r}_3 = (0,\ 0,\ 0)^T \\ \boldsymbol{r}_4 = (0,\ l_0, -l_1)^T \\ \boldsymbol{r}_5 = (0,\ l_0, -l_2 - l_1)^T \end{cases}. \tag{4}$$

In Formula (2), the initial pose of the tool coordinate system $\{T\}$ is shown in Formula (5).

$$g_{st}(\mathbf{0}) = \begin{pmatrix} \boldsymbol{I}_{3\times3} & \begin{pmatrix} 0 \\ l_0 \\ -l_0 - l_1 - l_2 \end{pmatrix} \\ \mathbf{0} & 1 \end{pmatrix}. \tag{5}$$

Substituting formula (1) into formula (2), we can derive the relationship of p_1 and θ_4, as in Formula (6).

$$p_1 = \frac{ab}{\sqrt{(b\cos(\theta_4))^2 + (a\sin(\theta_4))^2}} - a. \tag{6}$$

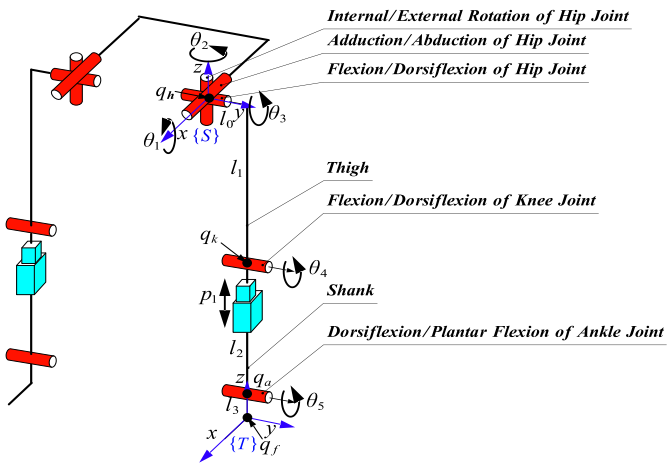


Figure 7. Kinematics coordinate system of the exoskeleton.

2.3.2. Inverse Kinematics

Through inverse kinematics allows us to find the hip, knee, and ankle joint angles if the orientations and positions of the tool coordinate system $\{T\}$ are given. We set up and solved the inverse kinematics by solving the Paden–Kahan subproblem [28].

The first Paden–Kahan subproblem involves rotation about a single axis. Let p represent the point before rotation, and q denote the point that has been rotated by an angle θ with respect to the axis vector $\boldsymbol{S}$. A circle is traced along the path of point q, as illustrated in Figure 8a. The vector $\boldsymbol{S}$, which has a magnitude of 1, indicates the direction of rotation. The rotation angle θ for solving the inverse kinematics problem can be derived in Formula (7):

$$\theta = \text{atan2}\left(\boldsymbol{S}\cdot\left(\boldsymbol{u}_p \times \boldsymbol{v}_p\right), \boldsymbol{u}_p \cdot \boldsymbol{v}_p\right), \tag{7}$$

where $\boldsymbol{u}$ is a vector from a point on the axis vector $\boldsymbol{S}$ to point p. $\boldsymbol{v}$ is a vector from this point on the axis vector $\boldsymbol{S}$ to point q. $\boldsymbol{u}_p$ and $\boldsymbol{v}_p$ are the projection of $\boldsymbol{u}$ and $\boldsymbol{v}$ onto the plane, which is perpendicular to $\boldsymbol{S}$. atan2 is the arctangent2 function, which is covered in the range of −180 deg to 180 deg.

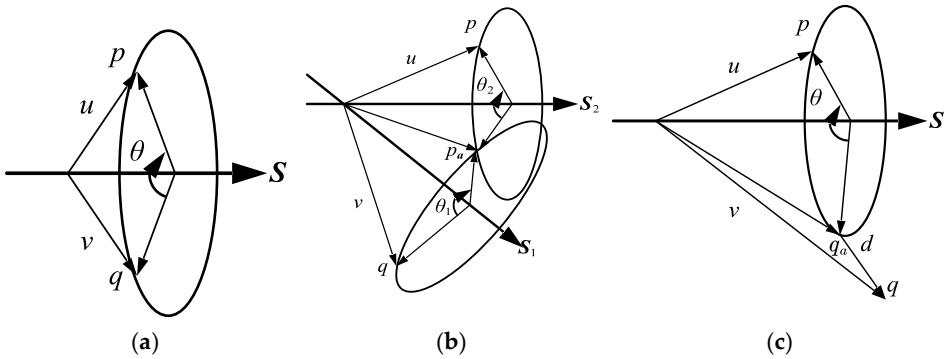


Figure 8. Paden–Kahan definition of inverse kinematics: (**a**) first subproblem; (**b**) second subproblem; (**c**) third subproblem.

The second Paden–Kahan subproblem is rotation about two subsequent axes, as shown in Figure 8b. p is a point rotated about the axis vector $\boldsymbol{S_2}$ until it coincides with point p_a. p_a is then rotated about the axis vector $\boldsymbol{S_1}$ until it coincides with points q. To solve the inverse kinematics, p_a is determined by Formula (8):

$$p_a = \delta \boldsymbol{S_1} + \varepsilon \boldsymbol{S_2} + \sigma(\boldsymbol{S_1} \times \boldsymbol{S_2}), \tag{8}$$

where vectors S_1 and S_2 are unity vectors. δ, ε, and σ are given by

$$\delta = \frac{(S_1 \cdot S_2)(S_2 \cdot u) - S_1 \cdot v}{(S_1 \cdot S_2)^2 - 1}, \tag{9}$$

$$\varepsilon = \frac{(S_1 \cdot S_2)(S_2 \cdot v) - S_1 \cdot u}{(S_1 \cdot S_2)^2 - 1}, \tag{10}$$

$$\sigma = \pm\sqrt{\|u\|^2 - \delta^2 - \varepsilon^2 - 2\delta\varepsilon(S_1 \cdot S_2)}, \tag{11}$$

By Formulas (8)–(11), the solution of inverse kinematics is from $e^{[S_2]\theta_2} p = p_a$ and $e^{[S_2]\theta_1} p_a = q$.

The third Paden–Kahan subproblem involves a point that rotates around an axis and then translates to a position, as illustrated in Figure 8c. Point p is rotated around axis S until it aligns with q_a. q_a translates d to point q along a line, which is tangent to the circle of the revolution path of point p. The solution of the third Paden–Kahan subproblem can be expressed as

$$\theta = atan2\left(S \cdot (u_p \times v_p), u_p \cdot v_p\right) \pm acos\left(\frac{\|u_p\|^2 + \|v_p\|^2 - d^2}{2\|u_p\|\|v_p\|}\right), \tag{12}$$

where u_p, v_p, and d_p are projections u, v, and d onto the plane that is perpendicular to S, respectively.

Establishing an inverse kinematics model about the exoskeleton satisfies the above three subproblems. Based on Formula (2), we defined g_0 as

$$g_0 = g_{st}(\theta) g_{st}^{-1}(0) = e^{[\hat{\xi}_1]\theta_1} e^{[\hat{\xi}_2]\theta_2} e^{[\hat{\xi}_3]\theta_3} e^{[\hat{\xi}_4]\theta_4} e^{[\hat{\xi}_5]\theta_5} e^{[\hat{\xi}_6]p_1}. \tag{13}$$

q_f represents the original point in coordinate system $\{T\}$, and q_a denotes the intersection point between the shank and foot at the axis of the ankle joint. Define $q_f{}'$ as the transformed position of q_f, and $q_a{}'$ as the transformed position of q_a. Based on Figure 7, the distance between $q_f{}'$ and $q_a{}'$ is described as follows:

$$\left\| q_f{}' - q_a{}' \right\| = \left\| q_f - q_a \right\| = l_3. \tag{14}$$

According to the first Paden–Kahan subproblem, we substituted Formula (13) into Formula (14) and obtained Formula (15).

$$\left\| g_0 q_f - g_0 e^{-[\hat{\xi}_5]\theta_5} q_a \right\| = \left\| g_0 \left(q_f - q_a \right) \right\|. \tag{15}$$

We substituted u_5 and v_5 as u_p and v_p, respectively. The vectors u_5 and v_5 are set on the plane where l_2 and l_3 are intersecting. The vector coordinates that are related to the ankle joint are derived as

$$u_5 = q_f - q_a = (0,\ 0,\ -l_3)^T, \tag{16}$$

$$v_5 = q_f' - q_a' = (m_5,\ 0,\ n_5)^T, \tag{17}$$

where m_5 and n_5 fulfill the following equation.

$$\sqrt{{m_5}^2 + {n_5}^2} = l_3. \tag{18}$$

Based on Formulas (15)~(18), θ_5 is

$$\theta_5 = \begin{cases} atan2(\hat{\omega}_5 \cdot (\boldsymbol{u}_5 \times \boldsymbol{v}_5), \boldsymbol{u}_5 \cdot \boldsymbol{v}_5) \\ \frac{\pi}{2} - atan2(m_5, n_5) \end{cases}. \tag{19}$$

We solve the rotation angle θ_4 and define q_k as the point of intersection between the shank and thigh at the axis of the knee joint. ${q_k}'$ is defined as the point q_k after transformation, and we define g_1 as

$$g_1 = g_{st}(\boldsymbol{\theta}) g_{st}^{-1}(\mathbf{0}) e^{-[\hat{\xi}_5]\theta_5} = e^{[\hat{\xi}_1]\theta_1} e^{[\hat{\xi}_2]\theta_2} e^{[\hat{\xi}_3]\theta_3} e^{[\hat{\xi}_4]\theta_4} e^{[\hat{\xi}_6]p_1}. \tag{20}$$

Based on Figure 7, the distance between ${q_k}'$ and ${q_a}'$ is

$$\left\| {q_a}' - {q_f}' \right\| = l_2 + p_1. \tag{21}$$

Based on the third Paden–Kahan subproblem, substituting Formula (20) into (21), we derived

$$\left\| g_1 q_a - g_1 e^{-[\hat{\xi}_4]\theta_4} e^{-[\hat{\xi}_6]p_1} q_k \right\| = \left\| e^{[\hat{\xi}_6]p_1} q_a - q_k \right\|. \tag{22}$$

We substituted $\boldsymbol{u}_4$ and $\boldsymbol{v}_4$ as $\boldsymbol{u}_p$ and $\boldsymbol{v}_p$, respectively. The vector $\boldsymbol{u}_4$ and $\boldsymbol{v}_4$ are set on the plane where l_1 and l_2 are intersecting. We defined the vector coordinate that is related on the knee joint as

$$\boldsymbol{u}_4 = q_a - q_k = (0, 0, -l_2 - p_1)^T, \tag{23}$$

$$\boldsymbol{v}_4 = q_a' - q_k' = (m_4,\ 0,\ n_4)^T, \tag{24}$$

where

$$\sqrt{{m_4}^2 + {n_4}^2} = l_2 + p_1. \tag{25}$$

We define d as

$$d = \|\boldsymbol{v}_4 - \boldsymbol{u}_4\|. \tag{26}$$

Based on Formulas (20)–(25), θ_4 is

$$\theta_4 = \begin{cases} atan2(\hat{\omega}_4 \cdot (\boldsymbol{u}_4 \times \boldsymbol{v}_4), \boldsymbol{u}_4 \cdot \boldsymbol{v}_4) \pm acos\left(\frac{\|\boldsymbol{u}_4\|^2 + \|\boldsymbol{v}_4\|^2 - d^2}{2\|\boldsymbol{u}_p\| \|\boldsymbol{v}_p\|} \right) \\ \frac{\pi}{2} - atan2(m_4, n_4) \end{cases}. \tag{27}$$

We define q_h as the center of the hip joint. Based on Figure 7 and Formula (13), the distance between ${q_k}'$ and q_h can be derived as

$$\left\| {q_k}' - q_h \right\| = \left\| e^{[\hat{\xi}_1]\theta_1} e^{[\hat{\xi}_2]\theta_2} e^{[\hat{\xi}_3]\theta_3} q_k - q_h \right\| = \|q_k - q_h\| = \sqrt{{l_0}^2 + {l_1}^2}. \tag{28}$$

Based on the second Paden–Kahan subproblem, we defined the process of solving $\boldsymbol{\theta_1}$, $\boldsymbol{\theta_2}$, and $\boldsymbol{\theta_3}$ as follows: Point $\boldsymbol{q_k}$ is rotated along $\boldsymbol{\theta_1}$ until it is aligned with $\boldsymbol{q_k''}$; then, $\boldsymbol{q_k''}$ is rotated along $\boldsymbol{\theta_2}$ until it is aligned with $\boldsymbol{q_k'''}$; finally, $\boldsymbol{q_k'''}$ is rotated along $\boldsymbol{\theta_3}$ until it is aligned with $\boldsymbol{q_k'}$. Based on Formula (2), we derived.

$$\boldsymbol{u}_1 = q_k - q_h = (0, l_0, -l_1)^T, \tag{29}$$

$$\boldsymbol{p}_{a1} = q_k'' - q_h = (0,\ m_1,\ n_1)^T, \tag{30}$$

$$\boldsymbol{u}_2 = \boldsymbol{p}_{a1} = (0,\ m_1,\ n_1)^T, \tag{31}$$

$$\boldsymbol{p}_{a2} = q_k''' - q_h = (m_2,\ n_2,\ s_2)^T, \tag{32}$$

$$\boldsymbol{v}_1 = \boldsymbol{p}_{a2} = (m_2,\ n_2,\ s_2)^T, \tag{33}$$

$$\boldsymbol{v}_2 = q_k' - q_h = (m_3,\ s_3,\ n_3)^T. \tag{34}$$

where $\boldsymbol{p_{a1}}$ and $\boldsymbol{u_2}$ are the vectors which are exactly equal and which are both point from $\boldsymbol{q_h}$ to $\boldsymbol{q_k''}$. $\boldsymbol{p_{a2}}$ and $\boldsymbol{v_1}$ are the vectors which are exactly equal and which are both point from $\boldsymbol{q_h}$ to $\boldsymbol{q_k'''}$. $\boldsymbol{u_1}$ is the vectors point from $\boldsymbol{q_h}$ to $\boldsymbol{q_k}$ and $\boldsymbol{v_2}$ is the vectors point from $\boldsymbol{q_h}$ to $\boldsymbol{q_k'}$ Based on Formulas (8)–(11), we obtained

$$q_k'' = \delta_1 \hat{\omega}_2 + \varepsilon_1 \hat{\omega}_1 + \sigma_1(\hat{\omega}_2 \times \hat{\omega}_1), \tag{35}$$

$$q_k''' = \delta_2 \hat{\omega}_3 + \varepsilon_2 \hat{\omega}_2 + \sigma_2(\hat{\omega}_3 \times \hat{\omega}_2), \tag{36}$$

where

$$\delta_2 = \frac{(\hat{\omega}_3 \cdot \hat{\omega}_2)(\hat{\omega}_3 \cdot \boldsymbol{u}_2) - \hat{\omega}_3 \cdot \boldsymbol{v}_2}{(\hat{\omega}_2 \cdot \hat{\omega}_3)^2 - 1}, \tag{37}$$

$$\delta_1 = \frac{(\hat{\omega}_2 \cdot \hat{\omega}_1)(\hat{\omega}_2 \cdot \boldsymbol{u}_1) - \hat{\omega}_2 \cdot \boldsymbol{v}_1}{(\hat{\omega}_1 \cdot \hat{\omega}_2)^2 - 1}, \tag{38}$$

$$\varepsilon_2 = \frac{(\hat{\omega}_3 \cdot \hat{\omega}_2)(\hat{\omega}_2 \cdot \boldsymbol{v}_2) - \hat{\omega}_3 \cdot \boldsymbol{u}_2}{(\hat{\omega}_2 \cdot \hat{\omega}_3)^2 - 1}, \tag{39}$$

$$\varepsilon_1 = \frac{(\hat{\omega}_2 \cdot \hat{\omega}_1)(\hat{\omega}_1 \cdot \boldsymbol{v}_1) - \hat{\omega}_2 \cdot \boldsymbol{u}_1}{(\hat{\omega}_1 \cdot \hat{\omega}_2)^2 - 1}, \tag{40}$$

$$\sigma_1 = \pm\sqrt{\|\boldsymbol{u}_1\|^2 - {\delta_1}^2 - {\varepsilon_1}^2 - 2\delta_1\varepsilon_1(\hat{\omega}_2 \cdot \hat{\omega}_1)}, \tag{41}$$

$$\sigma_2 = \pm\sqrt{\|\boldsymbol{u}_2\|^2 - {\delta_2}^2 - {\varepsilon_2}^2 - 2\delta_2\varepsilon_2(\hat{\omega}_3 \cdot \hat{\omega}_2)}. \tag{42}$$

Based on the second Paden–Kahan subproblem and Formulas (28)–(42), the solutions of $\boldsymbol{\theta_1}$, $\boldsymbol{\theta_2}$, and $\boldsymbol{\theta_3}$ can be derived by

$$\begin{cases} e^{[\hat{\omega}_1]\theta_1} q_k = q_k'' \\ e^{[\hat{\omega}_2]\theta_2} q_k'' = q_k''' \\ e^{[\hat{\omega}_3]\theta_3} q_k' = q_k''' \end{cases}. \tag{43}$$

2.4. Simulation and Workspace of Exoskeleton

2.4.1. Walking Simulation of Exoskeleton

We imported the virtual model of the exoskeleton and a human model to conduct virtual simulations via ADAMS. This human model was designed with a height of 170 cm and a weight of 70 kg. The assistance provided by lower limb exoskeletons to the legs during walking was simulated. We adjusted the human model to a standing posture and connected it with the exoskeleton. The hip, knee, and ankle joints of the exoskeleton module were activated, connecting the thighs, shanks, and feet in the human model to the exoskeleton. A ground was added beneath the human–machine system, and contact was established between the exoskeleton and ground. The configuration is shown in Figure 9.

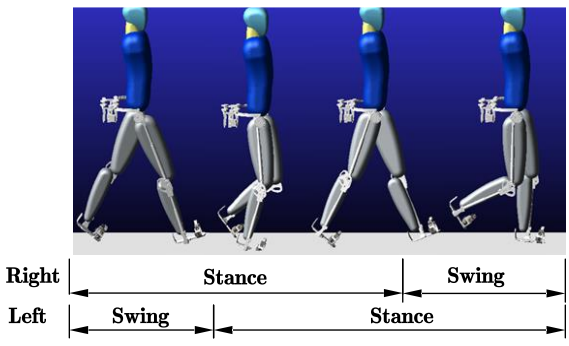


Figure 9. Simulation process of human wearing the exoskeleton to walk.

We imported the data obtained from OpenSim 4.3 to drive the joints to get the motion path coordinates of the foot in relation to the human–machine system. The theoretical motion path coordinates of foot motion were derived based on a previously established kinematic model. The paths are shown in Figure 10.

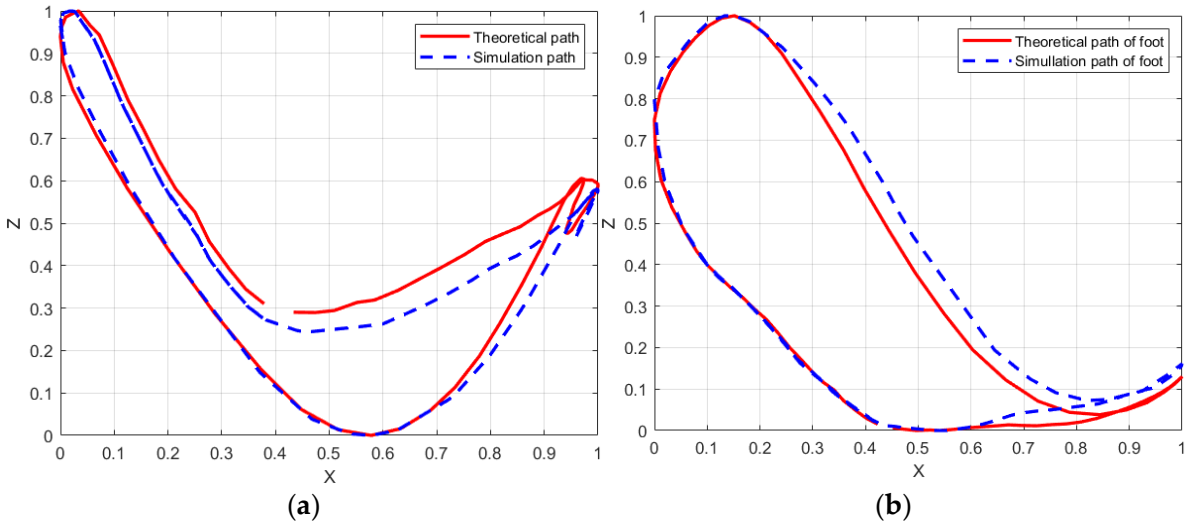


Figure 10. Comparation between simulation and theoretical path during walking locomotion: (**a**) path of knee joint; (**b**) path of foot joint.

We evaluated their similarity by calculating their Hausdorff distance, considering that the paths are not fitted into a function. The calculation of Hausdorff distance involves two directions, namely the distance from set A to set B (forward Hausdorff distance) and the distance from set B to set A (backward Hausdorff distance). The two distances are usually not equal. The calculation formula of the two Hausdorff distances is as follows.

$$h(A,\ B) = max(a \in A)min(b \in B)\|a - b\|, \tag{44}$$

$$h(B,\ A) = max(b \in B)min(a \in A)\|a - b\|, \tag{45}$$

where the Hausdorff distance is the maximum of the two distances.

The Hausdorff distance between the theoretical and simulated paths of the knee joint is 0.0643, and the Hausdorff distance between the theoretical and simulated paths of the foot is 0.1305. These results show a significant degree of similarity between both simulation and theory paths, thereby validating the rationality of the design of the exoskeleton at a theoretical level.

2.4.2. Workspace of Walking Locomotion

The exoskeleton workspace was defined to ensure that the wheelchair structure within the system did not interfere walking. The calculation of the exoskeleton workspace was based on the kinematic model and joint rotation angles established by the International Society of Biomechanics, as shown in Figure 11. We observed that the maximum space occupied by the backward swing of leg was approximately 430 mm, and the trunk experienced a vertical movement of about 100 mm during walking locomotion.

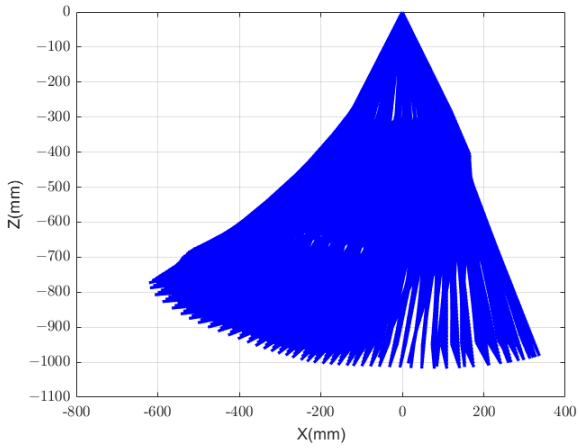


Figure 11. The workspace of the lower extremity exoskeleton on the sagittal plane during walking.

3. Design and Analysis of STS Assistive Mechanism

3.1. Analysis of STS Process

The STS assistive mechanism is designed based on the analysis of human STS transfer motion. Li et al. [18] categorized the STS movement of healthy adults into four distinct stages based on changes in shank locomotion direction, as shown in Figure 12.

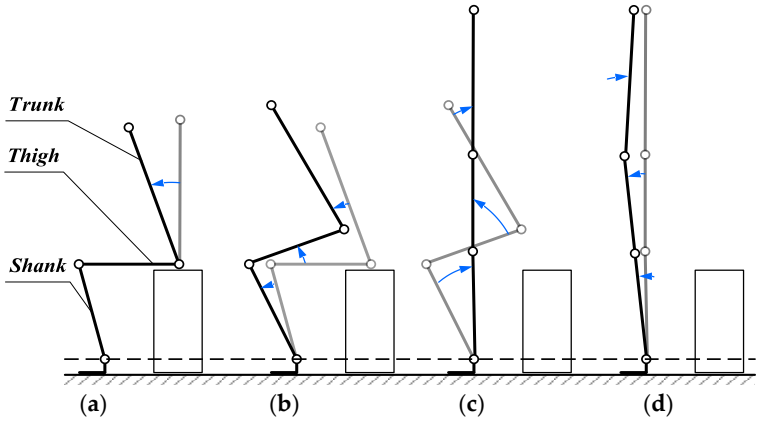


Figure 12. The process of STS motion of heathy human: (**a**) initial stage; (**b**) balance stage; (**c**) rising stage; (**d**) stabilization stage.

The details of the four stages are as follows:

1. Initial stage: The human trunk rotates forward around the flexion/extension axis of the hip joint until the hips disengage from the seat.
2. Balance stage: As the buttocks leave the seat, the entire body leans forward about the axis of the ankle joint.
3. Rising stage: The shank rotates backward about the axis of the ankle joint, the thigh rotates forward about the axis of the knee joint, and the trunk rotates backward about the axis of the hip flexion/extension until the body achieves a vertical position.
4. Stabilization stage: Both shanks and thighs are slightly tilted forward concurrently to maintain stability over the center of gravity.

The findings conducted by Reznick et al. [29] demonstrated that the overall movement path of buttocks during STS transfer movement is consistent. We served the motion path coordinates of the hip joint, represented in a Cartesian coordinate system, as the path of the buttocks during this transfer. The normalized coordinates of the motion path for the human hip joint are illustrated in Figure 13.

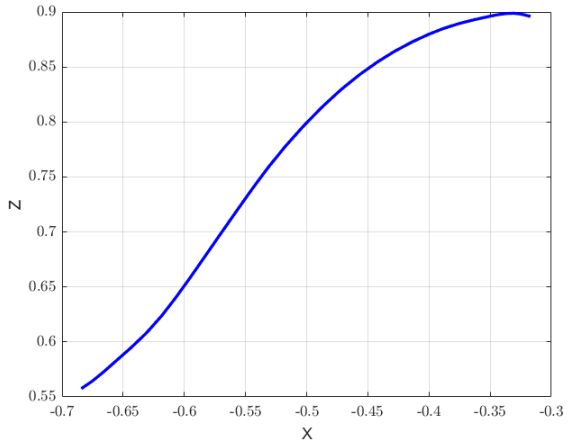


Figure 13. Coordinate variation in the hip joint on the sagittal plane during STS locomotion [29].

3.2. Design of STS Assistive Mechanism

3.2.1. Development of Path Synthesis Equation

The STS assistive mechanism facilitates the transfer movement by pushing the buttocks. We aligned a target point on the mechanism with the path of the hip joint during the STS process to design the STS assistive mechanism [30]. We found that the motion path of a point in a planar four-bar linkage can conform to this path based on paper [31], as shown in Figure 14a. We adopted an RR chain as support for the four-bar mechanism and integrated it to generate a Stephenson III six-bar mechanism, as shown in Figure 14b. The three-dimensional configuration diagram of the STS assistive mechanism was depicted in Figure 15.

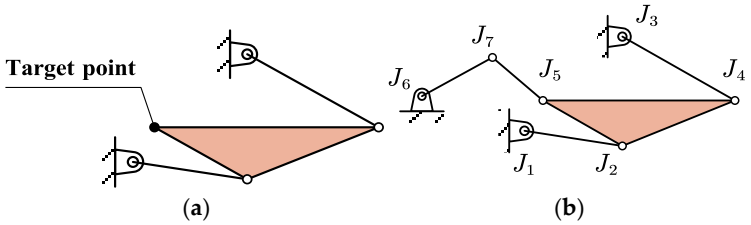


Figure 14. Simplified diagram of the linkage mechanism: (**a**) planar four-bar linkage; (**b**) Stephenson III six-bar mechanism.

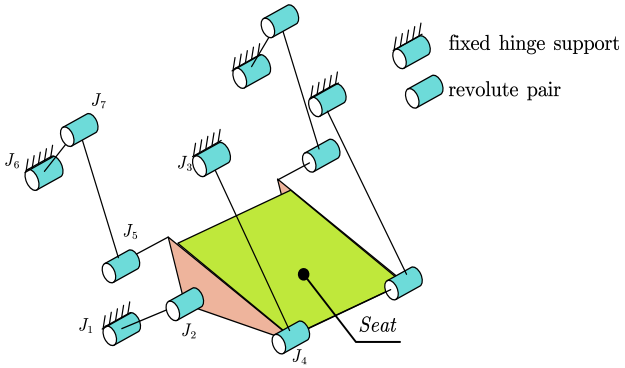


Figure 15. The configuration of the STS assistive mechanism.

We defined the target point as J_5 in the Stephenson III planar six-bar mechanism to align with the motion path of the human hip joint, as illustrated in Figure 16. A representative point along the hip joint's motion path during sit-to-stand (STS) movements served as target points for fitting by point J_5. Consequently, we designed this mechanism

by the path synthesis of point J_5. To facilitate movement, we connected the seat to linkage $J_4J_5J_2$ to assist pushing the patient's buttocks.

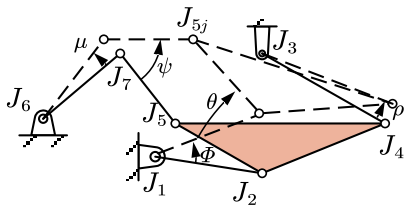


Figure 16. The STS assistive mechanism with the indication of the motion process.

J_1, J_2, J_3, J_4, and J_5 are complex vectors that represent the position of the revolute pair of the mechanism. According to the vector closed-loop equation, we obtained

$$\begin{cases} (J_2 - J_1) + (J_5 - J_2) = J_5 - J_1 \\ (J_4 - J_3) + (J_5 - J_4) = J_5 - J_3 \\ (J_7 - J_5) + (J_6 - J_7) = J_6 - J_5 \end{cases}. \tag{46}$$

The position of point J_5 is served as J_{5j} during the STS process. The following equation is obtained:

$$\begin{cases} e^{i\varphi_j}(J_2 - J_1) + e^{i\theta_j}(J_5 - J_2) = J_{5j} - J_1 \\ e^{i\rho_j}(J_4 - J_3) + e^{i\theta_j}(J_5 - J_4) = J_{5j} - J_3 \\ e^{i\psi_j}(J_7 - J_5) + e^{i\mu_j}(J_6 - J_7) = J_6 - J_{5j} \\ j = 1, \ldots, N \end{cases}. \tag{47}$$

The complex conjugate equation is

$$\begin{cases} e^{-i\varphi_j}\left(\overline{J}_2 - \overline{J}_1\right) + e^{-i\theta_j}\left(\overline{J}_5 - \overline{J}_2\right) = \overline{J}_{5j} - \overline{J}_1 \\ e^{-i\rho_j}\left(\overline{J}_4 - \overline{J}_3\right) + e^{-i\theta_j}\left(\overline{J}_5 - \overline{J}_4\right) = \overline{J}_{5j} - \overline{J}_3 \\ e^{-i\psi_j}\left(\overline{J}_7 - \overline{J}_5\right) + e^{-i\mu_j}\left(\overline{J}_6 - \overline{J}_7\right) = \overline{J}_6 - J_{5j} \\ j = 1, \ldots, N \end{cases}. \tag{48}$$

The above formulas constitute the synthesis equation of the Stephenson III path generator. For N specified path points, we have seven complex vector joint unknowns and five joint angle unknowns, and together with their complex conjugates, we have a total of $14 + 5 * N$ unknowns. We obtain three complex loop equations and their conjugates, for a total of $6 * N$ equations. For the case of $N = 14$, the number of equations and unknowns is equal, which produces 84 quadratic equations and 84 unknowns.

The key of this Stephenson III six-bar mechanism is the path synthesis of the four-bar mechanism $J_1J_2J_3J_4J_5$. We regard the mechanism as an RR chain $\left(J_6J_7J_{5j},\ j = 1, \ldots, N\right)$ and a four-bar mechanism $J_1J_2J_3J_4J_5$. The motion of J_5 point is regarded as determined by the four-bar mechanism $J_1J_2J_3J_4J_5$. Therefore, we determined the size and joint coordinates of the RR chain $\left(J_6J_7J_{5j},\ j = 1, \ldots, N\right)$, and we mainly calculated the four-bar mechanism $J_1J_2J_3J_4J_5$ to reduce the complexity of the synthesis equation of the Stephenson III path generator. We obtain $J_k = a_k + b_k i$ and $k = 1,\ 2,\ 3,\ 4,\ 5,\ 5j$, and we write $e^{i\rho_j}$, $e^{i\theta_j}$, and $e^{i\varphi_j}$ into algebraic form. The real part and imaginary part of each equation are separated into new equations:

$$\begin{cases} (a_5 - a_4)cos(\theta_j) + (b_4 - b_5)sin(\theta_j) + (a_4 - a_3)cos(\rho_j) + (b_3 - b_4)sin(\rho_j) + a_3 - a_{5j} = 0 \\ (b_5 - b_4)cos(\theta_j) + (a_5 - a_4)sin(\theta_j) + (b_4 - b_3)cos(\rho_j) + (a_4 - a_3)sin(\rho_j) + b_3 - b_{5j} = 0 \\ (a_5 - a_2)cos(\theta_j) + (b_2 - b_5)sin(\theta_j) + (a_2 - a_1)cos(\varphi_j) + (b_1 - b_2)sin(\varphi_j) + a_1 - a_{5j} = 0 \\ (b_5 - b_2)cos(\theta_j) + (a_5 - a_2)sin(\theta_j) + (b_2 - b_1)cos(\varphi_j) + (a_2 - a_1)sin(\varphi_j) + b_1 - b_{5j} = 0 \\ j = 1, \ldots, N \end{cases}. \tag{49}$$

These equations have 10 joint coordinates unknowns in N task positions, $3N$ joint angles unknowns, and a total of $10 + 3N$ unknowns. The obtained equations have a total of $4N$ equations. When $N = 10$, the number of equations is equal to the unknown number, and the equations have a definite solution. At this time, 40 nonlinear equations and 40 unknowns are generated. Moreover, the equations are nonlinear equations, and we can solve the equations via the Newton iteration method.

3.2.2. Solution of the Path Synthesis Equations

By creating a Newton iterative algorithm, Formula (49) is solved to obtain the coordinates of the joints of $J_1J_2J_3J_4J_5$ so as to obtain the length of each connecting rod in the four-bar mechanism $J_1J_2J_3J_4J_5$.

We select 10 points on the path curve as the 10 coordinates of the coupling point J_{5j} for path synthesis, as shown in Table 1. The coordinate points are substituted for the Newton iterative solution. J_{5_1} is taken as the initial point of J_5 to obtain the coordinate points shown in Table 2.

Table 1. Coordinates of J_{5j}.

j	**1**	**2**	**3**	**4**	**5**	**6**	**7**	**8**	**9**	**10**
a_{5j}	−457.7	−381.0	−322.2	−269.9	−222.9	−185.3	−143.5	−96.3	−32.5	22.2
b_{5j}	317.72	417	461.42	520.87	586.97	642.98	701.94	756.57	800.89	815.05

Table 2. Coordinates of J_1, J_2, J_3, J_4, and J_5.

	J_1	J_2	J_3	J_4	J_5
a_k	−351.4	−343.1	−132.9	18.8	−457.7
b_k	463.0	267.9	675.3	415.5	317.7

We specified the coordinates of the J_6 point and J_7 point as (−561, 810) and (−167.5, 782.26), respectively, and take the length of the connecting rod as shown in Table 3.

Table 3. Length of the Stephenson III six-bar mechanism.

Linkage	$\lvert J_1J_2\rvert$	$\lvert J_2J_4\rvert$	$\lvert J_3J_4\rvert$	$\lvert J_4J_5\rvert$	$\lvert J_5J_7\rvert$	$\lvert J_6J_7\rvert$
Length (mm)	193	277	310	477	260	155

3.2.3. Structure of STS Assistive Mechanism

We set up the whole STS assistive mechanism, as shown in Figure 17a. We connected the joint J_5 to the backrest. To ensure that the backrest remains vertical to the ground to keep patient's trunk stable during STS movement, we made the RR chain as the parallelogram mechanism connecting it to the backrest. We installed a safety belt on the backrest to enhance patient safety while allowing for free trunk tilting during STS transfer movements. To provide sufficient torque for driving STS motion, based on the weight of adults, we chose a BMXL linear actuator (travel: 250 mm; maximum force: 1000 N) produced in China to connect to J_1J_2. Figure 17b shows the prototype of the STS assistive mechanism.

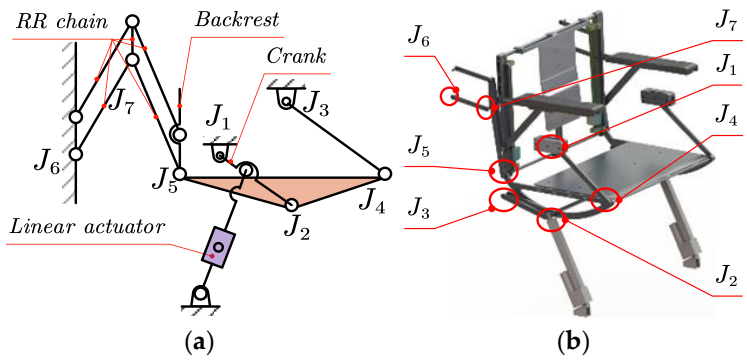


Figure 17. The STS assistive mechanism: (**a**) simplified diagram of the STS assistive mechanism; (**b**) prototype of the STS assistive mechanism.

3.2.4. Combination of Wheelchair and STS Assistive Mechanism

We combined the mechanism with the wheelchair after determining the dimensions of the STS assistive mechanism. J_1, J_3, J_6, J_7, and the linear actuator were affixed to the wheelchair frame, as shown in Figure 18b. The wheelchair frame as shown in Figure 18a measured 1090 mm in length and 600 mm in width. The material of the wheelchair frame is cast iron SS400, which is used to stabilize the system by increasing the weight of the frame.

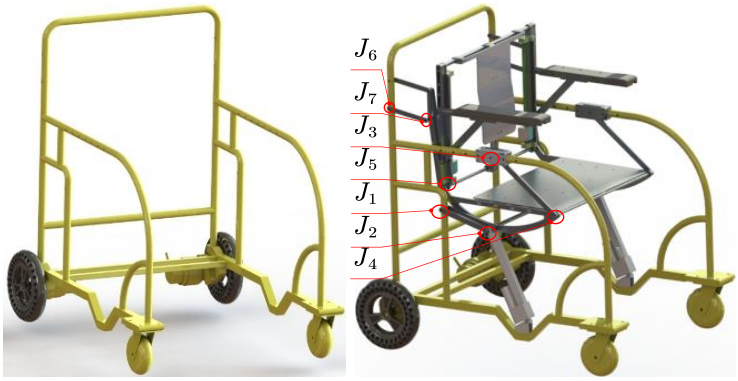
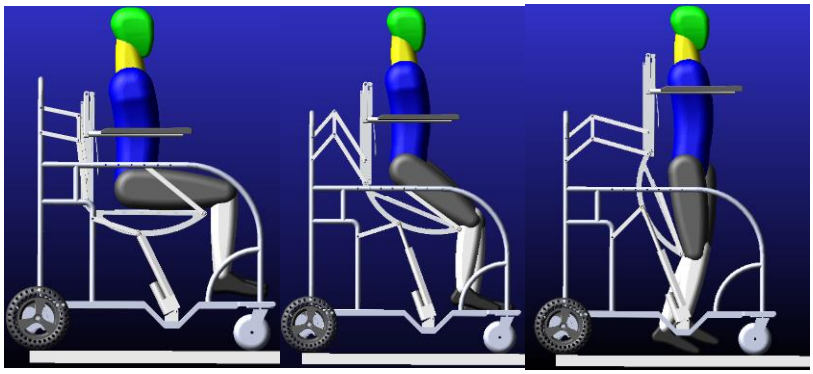


Figure 18. Structure of wheelchair: (**a**) prototype diagram of the wheelchair frame; (**b**) prototype diagram of wheelchair.

3.2.5. STS Simulation

STS transfer movement simulation was conducted to validate the STS assistive mechanism using ADAMS (Adams View 2020). We adjusted the body posture to a seated position and aligned it with the seat of the mechanism, as shown in Figure 19. We enabled the linear actuator to extend 120 mm within a duration of 10 s. The purpose of this simulation was to translate human models from a seated posture to a standing posture via the STS assistive mechanism. We normalized the obtained coordinate data for comparisons between the simulation and theory motion path of hip joints during an actual STS process, as shown in Figure 20. The Hausdorff distance was 0.0411, which indicated that the hip joint motion path during the simulated STS motion is highly similar to its theoretical motion path, theoretically confirming the rationality of the designed STS assistive mechanism.



(**a**) (**b**) (**c**)

Figure 19. Schematic diagram of the STS simulation: (**a**) sitting posture; (**b**) process of sit-to-stand transfer; (**c**) standing posture.

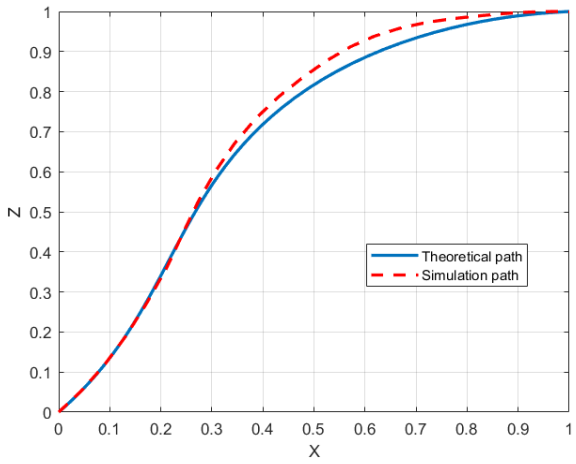


Figure 20. Comparison between simulated and theoretical path of the hip joint during the STS process.

3.3. Integration of the STS Assistive Mechanism and the Exoskeleton

We connected the exoskeleton to the STS assistive mechanism through a cylindrical slide rail installed on the backrest. The connection of the exoskeleton to the backrest via this slide rail enables it to be compatible with the vertical translational movement of the trunk when the wearer is engaged in the walking motion, as depicted in Figure 21.

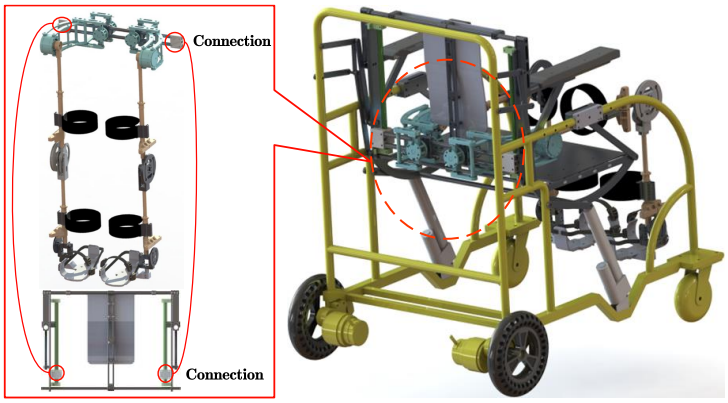


Figure 21. Integration of the exoskeleton and STS assistive mechanism.

We established the system of the entire device through the integration of the wheelchair, the STS assistive device, and the lower limb exoskeleton, as shown in Figure 22. The device has three models: sitting, standing, and walking. In the sitting posture, the device realizes

the function of assisting the patient to move from one place to another place. In the standing posture, the exoskeleton assists the swinging motion of the patient's lower limbs, while the entire system synchronizes with the walking speed of the human body. The conversion between the sitting and standing posture is assisted by the STS assistive mechanism.



(**a**) (**b**) (**c**)

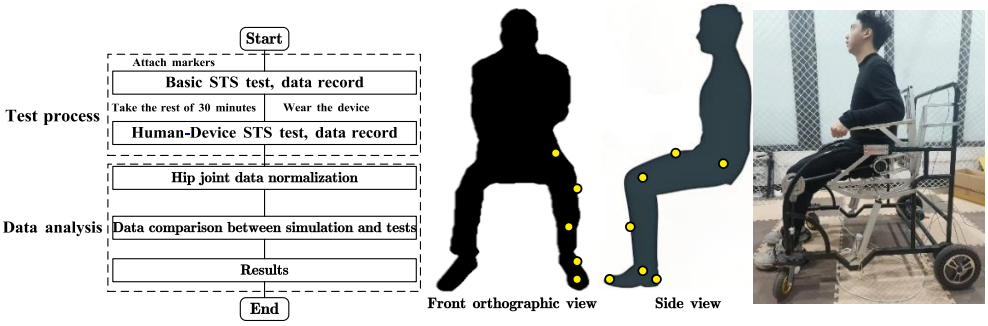
Figure 22. System model: (**a**) sitting model; (**b**) standing model; (**c**) walking model.

4. STS and Walking Experiments

4.1. STS Movement Experiments

4.1.1. Experiment Setup and Procedure

We conducted 3D motion capture experiments on STS assistive mechanisms to further investigate whether the STS assistive mechanism facilitated the execution of STS movements in a natural posture. The experimental scheme is shown in Figure 23a. Five healthy participants with a height of 170 ± 5 cm were selected for this study. To observe the movements of the participant's lower limb joints, marker balls were affixed to their left leg, as depicted in Figure 23b. The positions of the marker balls were captured and recorded by the VICON motion capture system.



(**a**) (**b**) (**c**)

Figure 23. STS experiment preparation: (**a**) test scheme; (**b**) attached marker balls; (**c**) participant test.

The participants performed ten STS exercise tests without any assistance from the device (basic STS test). After enough rest, i.e., 30 min, the participants performed ten STS exercise tests with the STS assistive mechanism's assistance (human–device STS test), as shown in Figure 23c. Data that regarded the hip joint positions of two groups of experiment were recorded to evaluate whether the STS assistive function of the device aligns with participant's STS movement posture.

4.1.2. Experimental Results

The hip positions of the participants collected during the experiment were normalized and compared with the hip position obtained from simulations, as shown in Figure 24. The Hausdorff distance between the path of the hip joint in the simulation and the path of the participant's hip joint during STS movements without assistance was 0.0872, and the distance between the motion path in simulation and the motion path of the participant's hip during STS movements with assistance by devices was 0.0413.

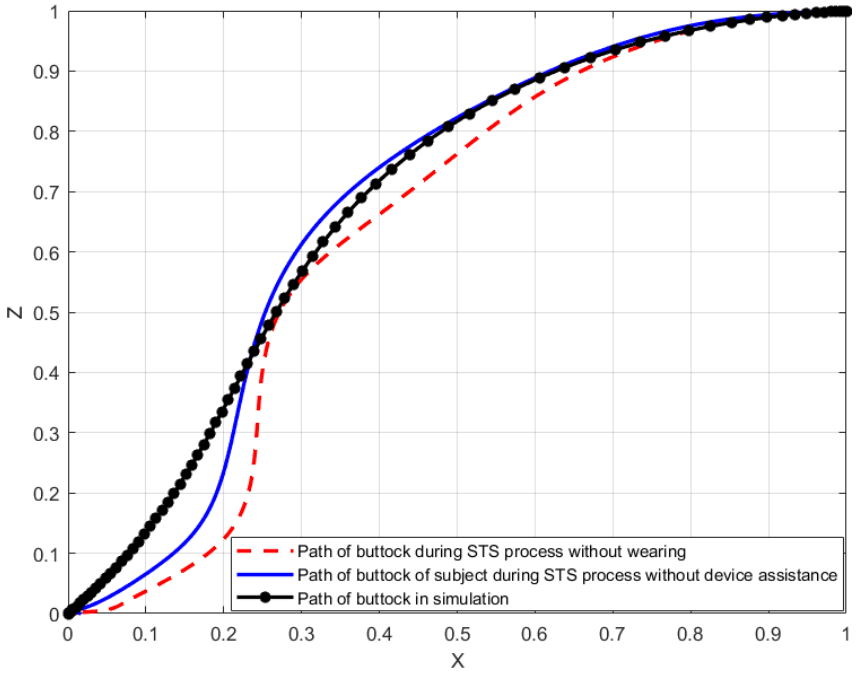


Figure 24. The comparison path of the buttock.

We found that the deviation was small by calculating the Hausdorff distance. The experimental results indicated that the trend in the motion path of the knee joint and foot in the test was consistent with that in the simulation. This finding indicated that the STS assistive mechanism provided assistance to STS movements, with postures aligned with those of healthy humans. The deviation between the path of the marked ball affixed to the human hip and the path of the hip in the simulation might be produced by soft human skin, etc., which had little effects on our test.

4.2. Walking Assistance Experiments

4.2.1. Experimental Setup and Procedure

We conducted 3D motion capture experiments on the exoskeleton to further investigate whether the device facilitates walking assistance in natural gaits. The experiment scheme is shown in Figure 25a. The healthy male participant with the height of 170 cm, as described in the STS experiment, was selected for this experiment. To observe the movements of the participant's lower limbs, marker balls were affixed to his left legs, as depicted in Figure 25b. The positions of the marker balls were captured and recorded by the VICON motion capture system.

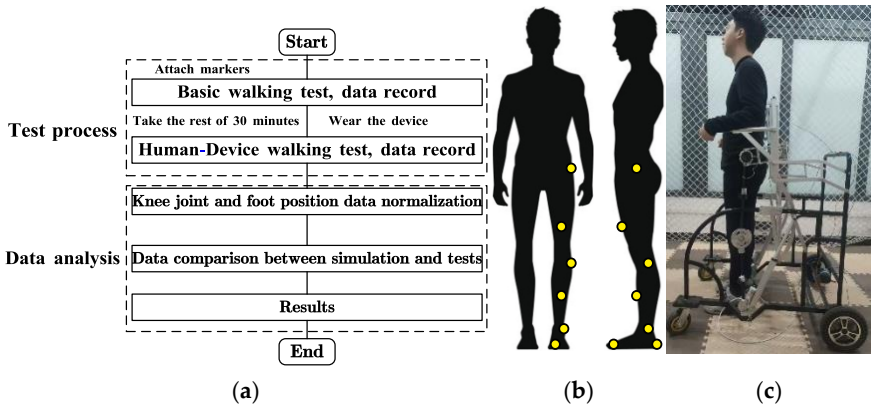


Figure 25. Walking experiment preparation: (**a**) test scheme; (**b**) attached marker balls; (**c**) participant test.

The participant performed walking experiments on a treadmill at a speed of 1 m/s for five trials without wearing the exoskeleton, with each lasting 10 s. After an enough rest, i.e., 30 min, the participant performed walking experiments on a treadmill at a speed of 1 m/s and the slope of 0 for five trials while wearing the device, as shown in Figure 25c, with each lasting 10 s. After enough rest, the participant performed walking experiments on a treadmill at a speed of 1 m/s and a slope of 15 deg for five trials while wearing the device, with each lasting 10 s. Data that regarded the knee joint and foot positions of the two groups of experiments were recorded to evaluate whether the assistive walking function of the device aligns with nature gaits.

4.2.2. Experimental Results

The knee joint and foot coordinates of the participant collected during the experiment were normalized and compared with those obtained from simulations, as shown in Figure 26. When walking on the treadmill at the slope of 0, for knee joints, the Hausdorff distance between the motion path in the simulation and that of the participant without wearing devices is 0.1257, and the distance between the motion path in the simulation and that of the participant wearing devices is 0.0833. For the foot, the Hausdorff distance between the motion path in the simulation and that of the participant's foot without devices is 0.018, and the distance between the motion path in the simulation and that of the participant wearing devices is 0.0473. When walking on the treadmill at a slope of 0, for knee joints, the Hausdorff distance between the motion path of the participant's knee joint with and without wearing devices is 0.0518. For the foot, the Hausdorff distance between the motion path of the participant's foot without the device and that of the participant wearing the device is 0.0418.

We found that the deviation was small by calculating the Hausdorff distance. The results indicated that the trend in the motion path of the knee and foot in the test was consistent with that in the simulation. This finding demonstrated that the device satisfied human–machine motion compatibility, and it verified that our design could effectively provide walking assistance for humans. In addition, from the walking test, the wheelchair with the STS assistive mechanism had no interference relative to lower limbs. The deviation between the path of the human leg in the test and the path in simulations might be produced by the human–machine interaction structure, etc., on the exoskeleton, which had little effect on our test.

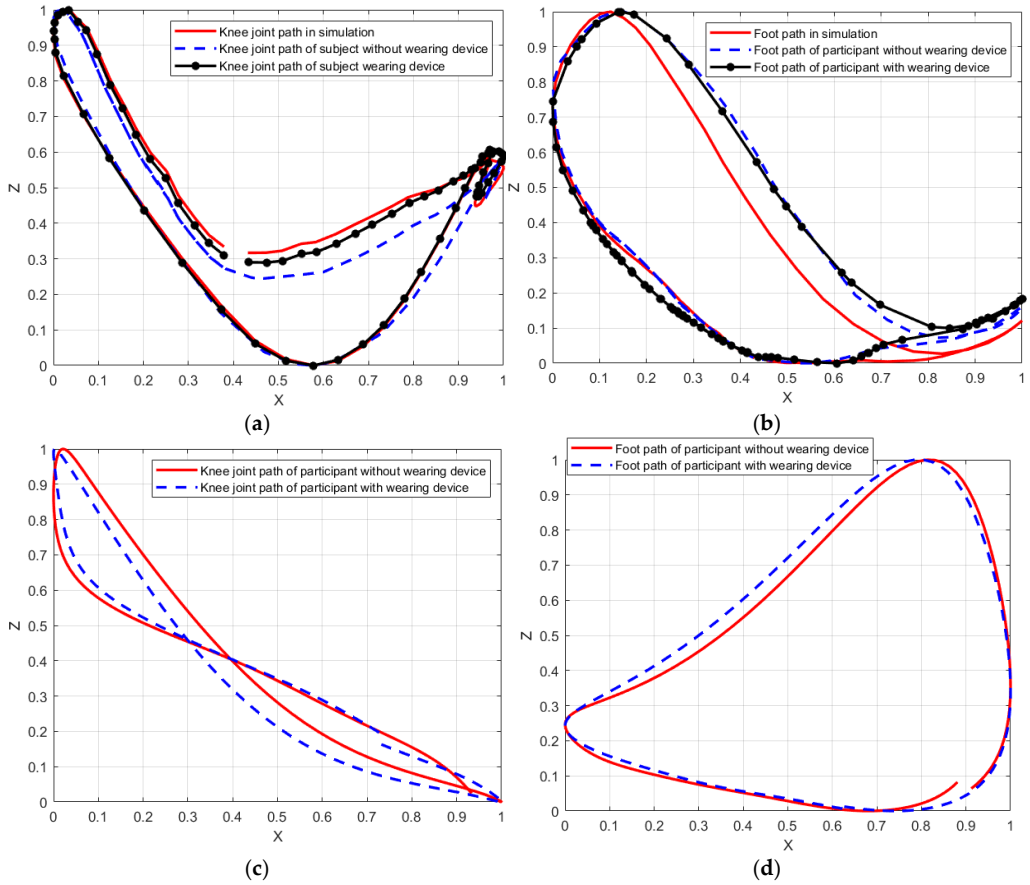


Figure 26. The path comparison of knee and ankle joints during walking experiments: (**a**) path coordinate of knee joint (slope is 0); (**b**) path coordinate of ankle joint (slope is 0). (**c**) Path coordinate of knee joint (slope is 15 deg); (**b**) path coordinate of ankle joint (slope is 15 deg).

5. Conclusions

This paper proposes a design of an innovative device that integrates a wheelchair, STS transfer movement, and lower limb exoskeleton function. The primary aim is to aid patients with lower limb dysfunction in STS movement and walking.

We designed a 10-degree-of-freedom lower limb exoskeleton based on gait analysis to facilitate walking locomotion and ensure human–machine compatibility. We designed the STS assistive mechanism based on the Stephenson III six-bar mechanism, and we utilized the path synthesis method to determine the size of the mechanism, which ensured that the assistance motion path of the STS assistive mechanism aligns with the human STS motion path. We connected the STS assistive mechanism to the wheelchair frame, and then, we connected the exoskeleton to the STS transfer assistive mechanism to integrate the function of walking, STS, and moving assistance. We conducted STS movement and walking assistance tests using a 3D motion capture system. The comparison results demonstrated that the device closely align with human movement trajectories, which validated the rationality of the STS movement and walking assistance function of our design.

The research presented in this paper offers a valuable reference for the design of lower limb assistive devices. In the future, we will devote research to the control algorithm for human–machine collaboration.

Author Contributions: All authors contributed to the conception and design of the research. Methodology investigation and preparation were performed by D.Y. The theoretical analysis and the first draft of the manuscript was carried out and written by B.L. and X.C. The experimental prototype was designed and produced by J.Z. The experiment was performed by H.L. and S.L. All authors com-

mented on previous versions of the manuscript. All authors have read and agreed to the published version of the manuscript.

Funding: Funding for this research was provided by the Chongqing Science and Technology Commission of China (cstc2020jcyj-msxmX0398), the Science and Technology Research Program of Chongqing Municipal Education Commission (KJZD-K202001103, KJQN202201169), and the Scientific Research Foundation of Chongqing University of Technology (2019ZD61).

Informed Consent Statement: Each subject provided written informed consent prior to participation in this study.

Data Availability Statement: The data presented in this study are included in the article. Further inquiries can be directed to the corresponding author.

Conflicts of Interest: The authors declare no conflicts of interest.

Abbreviations

The following abbreviations are used in this manuscript:

STS	Sit-to-stand;
POE	Product of exponential;
DOFs	Degrees of freedom;
RCM	Remote center of motion.

References

1. Hwang, B.; Jeon, D. A wheelchair integrated lower limb exercise/rehabilitation system: Design and experimental results on the knee joint. In Proceedings of the 2012 IEEE/SICE International Symposium on System Integration (SII), Fukuoka, Japan, 16–18 December 2012; pp. 164–169.
2. Suzuki, K.; Mito, G.; Kawamoto, H.; Hasegawa, Y.; Sankai, Y. Intention-based walking support for paraplegia patients with Robot Suit HAL. *Adv. Robot.* **2012**, *21*, 1441–1469. [CrossRef]
3. Desai, S.; Mantha, S.; Phalle, V. Design of a reconfigurable wheelchair with stand-sit-sleep capabilities for enhanced independence of long-term wheelchair users. *Technol. Disabil.* **2018**, *30*, 135–151. [CrossRef]
4. Sato, M.; Kannari, K.; Tomari, M.; Kawaguchi, T. Physical therapy intervention with a low frequency of exercise for a patient with a complicated form of hereditary spastic paraplegia: A case report. *J. Phys. Ther. Sci.* **2019**, *31*, 545–549. [CrossRef] [PubMed]
5. Pelletier, C. Exercise prescription for persons with spinal cord injury: A review of physiological considerations and evidence-based guidelines. *Appl. Physiol. Nutr. Metab.* **2023**, *48*, 882–895. [CrossRef]
6. Hsieh, L.-C.; Chen, T.-H. The Innovative Design and Prototype Verification of Wheelchair with One Degree of Freedom to Perform Lifting and Standing Functions. *IOP Conf. Ser. Mater. Sci. Eng.* **2017**, *280*, 012027. [CrossRef]
7. Meng, Q.; Jiang, M.; Jiao, Z.; Yu, H. Bionic design and analysis of a multi-posture wheelchair. *Mech. Sci.* **2022**, *13*, 1–13. [CrossRef]
8. Merai, S.; Shah, D.; Trivedi, B.; Joshi, P.; Kushwah, S. A study and design of standing wheelchair. *Mater. Today Proc.* **2022**, *65*, 3787–3792. [CrossRef]
9. Heins, S.; Flynn, L.L.; Laloyaux, H.; Geeroms, J.; Lefeber, D.; Ronsse, R. Compliant Control of a Transfemoral Prosthesis by combining Feed-Forward and Feedback. In Proceedings of the 2020 8th IEEE RAS/EMBS International Conference for Biomedical Robotics and Biomechatronics (BioRob), New York, NY, USA, 29 November–1 December 2020.
10. Lu, Z.; Ye, D.; Chen, Q.; Liu, C.; Dong, H.; Cheng, D. Adaptive Adjustment Strategy for Walking Characteristics of Single-Legged Exoskeleton Robots. *Machines* **2022**, *10*, 134. [CrossRef]
11. Jyräkoski, T.; Merilampi, S.; Puustinen, J.; Kärki, A. Over-ground robotic lower limb exoskeleton in neurological gait rehabilitation: User experiences and effects on walking ability. *Technol. Disabil.* **2021**, *33*, 53–63. [CrossRef]
12. Lee, H.; Rouse, E.J.; Krebs, H.I. Summary of Human Ankle Mechanical Impedance During Walking. *IEEE J. Transl. Eng. Health Med.* **2016**, *4*, 2100407. [CrossRef]
13. Rathore, A.; Wilcox, M.; Ramirez, D.Z.M.; Loureiro, R.; Carlson, T. Quantifying the human-robot interaction forces between a lower limb exoskeleton and healthy users. In Proceedings of the 38th Annual International Conference of the IEEE Engineering in Medicine and Biology Society (EMBC), Orlando, FL, USA, 16–20 August 2016; pp. 586–589.
14. Gurriet, T.; Tucker, M.; Duburcq, A.; Boeris, G.; Ames, A.D. Towards variable assistance for lower body exoskeletons. *IEEE Robot. Autom. Lett.* **2019**, *5*, 266–273. [CrossRef]
15. Liu, J.; He, Y.; Yang, J.; Cao, W.; Wu, X. Design and analysis of a novel 12-DOF self-balancing lower extremity exoskeleton for walking assistance. *Mech. Mach. Theory* **2022**, *167*, 104519. [CrossRef]

16. Song, Z.; Tian, C.; Dai, J.S. Mechanism design and analysis of a proposed wheelchair-exoskeleton hybrid robot for assisting human movement. *Mech. Sci.* **2019**, *10*, 11–24. [CrossRef]
17. Chaichaowarat, R.; Prakthong, S.; Thitipankul, S. Transformable Wheelchair–Exoskeleton Hybrid Robot for Assisting Human Locomotion. *Robotics* **2023**, *12*, 16. [CrossRef]
18. Li, J.; Xue, Q.; Yang, S.; Han, X.; Zhang, S.; Li, M.; Guo, J. Kinematic analysis of the human body during sit-to-stand in healthy young adults. *Medicine* **2021**, *100*, e26208. [CrossRef]
19. Das, S.; Halder, S.; Sahu, S.K.; Srinivasan, S.; Rakshit, S. Design and Development of a Sit-to-Stand Assistive Device. In *Machines, Mechanism and Robotics, Proceedings of the iNaCoMM 2019, Mandi, India, 5–7 December 2019*; Springer: Singapore, 2022; pp. 249–256.
20. Zhou, B.; Xue, Q.; Yang, S.; Wang, T. Design and Simulation of High-human-machine Cooperation Sit-to-Stand Assistive Device. In Proceedings of the 2020 3rd IEEE International Conference on Knowledge Innovation and Invention (ICKII), Kaohsiung, Taiwan, 21–23 August 2020; pp. 231–234.
21. Rea, P.; Ruggiu, M.; Ottaviano, E. Synthesis and Prototyping of a Sit-to-Stand Assisting Device. *Machines* **2024**, *12*, 33. [CrossRef]
22. Delp, S.L.; Anderson, F.C.; Arnold, A.S.; Loan, P.; Habib, A.; John, C.T.; Guendelman, E.; Thelen, D.G. OpenSim: Open-Source Software to Create and Analyze Dynamic Simulations of Movement. *IEEE Trans. Biomed. Eng.* **2007**, *54*, 1940–1950. [CrossRef]
23. Byrne, D.P.; Mulhall, K.J.; Baker, J.F. Anatomy & Biomechanics of the Hip. *Open Sports Med. J.* **2010**, *4*, 51–57. [CrossRef]
24. Wang, Z.; Zhang, W.; Ding, X. Design and analysis of a novel mechanism with a two-DOF remote centre of motion. *Mech. Mach. Theory* **2020**, *153*, 103990. [CrossRef]
25. Jiang, J.; Chen, P.; Peng, J.; Qiao, X.; Zhu, F.; Zhong, J. Design and Optimization of Lower Limb Rehabilitation Exoskeleton with a Multiaxial Knee Joint. *Biomimetics* **2023**, *8*, 156. [CrossRef]
26. Grothues, S.A.G.A.; Radermacher, K. Variation of the Three-Dimensional Femoral J-Curve in the Native Knee. *J. Pers. Med.* **2021**, *11*, 592. [CrossRef] [PubMed]
27. Hasan, S.K.; Dhingra, A.K. Biomechanical design and control of an eight DOF human lower extremity rehabilitation exoskeleton robot. *Results Control Optim.* **2022**, *7*, 100107. [CrossRef]
28. An, H.S.; Seo, T.W.; Lee, J.W. Generalized solution for a sub-problem of inverse kinematics based on product of exponential formula. *J. Mech. Sci. Technol.* **2018**, *32*, 2299–2307. [CrossRef]
29. Reznick, E.; Embry, K.R.; Neuman, R.; Bolívar-Nieto, E.; Fey, N.P.; Gregg, R.D. Lower-limb kinematics and kinetics during continuously varying human locomotion. *Sci. Data* **2021**, *8*, 282. [CrossRef]
30. Kamnik, R.; Bajd, T. Standing-up robot: An assistive rehabilitative device for training and assessment. *J. Med. Eng. Technol.* **2009**, *28*, 74–80. [CrossRef]
31. Purwar, A.; Bhargava, K.; Behan, E. A multi-functional mobility assist device for sit-to-stand motion. *Int. J. Ind. Ergon.* **2023**, *93*, 103396. [CrossRef]

Disclaimer/Publisher's Note: The statements, opinions and data contained in all publications are solely those of the individual author(s) and contributor(s) and not of MDPI and/or the editor(s). MDPI and/or the editor(s) disclaim responsibility for any injury to people or property resulting from any ideas, methods, instructions or products referred to in the content.